Corresponding author: V.V. Atuchin
Institute of Semiconductor Physics, Novosibirsk 630090, Russia
Phone: +7 (383) 3308889
E-mail: atuchin@isp.nsc.ru

High-Temperature Oxidation of Europium (II) Sulfide

Yu.G. Denisenko[1,2], M.S. Molokeev[3,4,5], A. S. Krylov[6], A.S. Aleksandrovsky[7,8], A.S. Oreshonkov[4,6]
V.V. Atuchin[9,10,11,12], N.A. Azarapin[1], P.E. Plusnin[13], E.I. Sal'nikova[1,14], O.V. Andreev[1]

[1]Institute of Chemistry, Tyumen State University, Tyumen 625003, Russia

[2]Department of General and Special Chemistry, Industrial University of Tyumen, Tyumen 625000, Russia

[3]Laboratory of Crystal Physics, Kirensky Institute of Physics, Federal Research Center KSC SB RAS, Krasnoyarsk 660036, Russia

[4]Siberian Federal University, Krasnoyarsk 660041, Russia

[5]Department of Physics, Far Eastern State Transport University, Khabarovsk 680021, Russia

[6]Laboratory of Molecular Spectroscopy, Kirensky Institute of Physics Federal Research Center KSC SB RAS, Krasnoyarsk 660036, Russia

[7]Laboratory of Coherent Optics, Kirensky Institute of Physics Federal Research Center KSC SB RAS, Krasnoyarsk 660036, Russia

[8]Institute of Nanotechnology, Spectroscopy and Quantum Chemistry, Siberian Federal University, Krasnoyarsk 660041, Russia

[9]Laboratory of Optical Materials and Structures, Institute of Semiconductor Physics, SB RAS, Novosibirsk 630090, Russia

[10]Functional Electronics Laboratory, Tomsk State University, Tomsk 634050, Russia

[11]Laboratory of Single Crystal Growth, South Ural State University, Chelyabinsk 454080, Russia

[12]Research and Development Department, Kemerovo State University, Kemerovo 650000, Russia

[13]Laboratory of Chemistry of Rare Platinum Metals, Nikolaev Institute of Inorganic Chemistry SB RAS, Novosibirsk, 630090, Russia

[14]Department of General Chemistry, Northern Trans-Ural Agricultural University, Tyumen, 625003, Russia

Abstract

The process of high-temperature oxidation of europium monosulfide EuS in air in the dynamic and isothermal regimes was expolored in the temperature range of 500-1000°C. According to the data of differential scanning calorimetry, the enthalpy of the complete oxidation reaction is established (ΔH^0_{exp} = −1718.5 kJ/mol), which has good convergence with the calculated value (ΔH^0_{calc} = −1731.1 kJ/mol). The study of oxidation products formed in the isothermal mode allowed us to establish the mechanism of europium monosulfide oxidation with air oxygen. EuS oxidation is a complex two-step process in combination with a large number of topochemical equilibria. In the temperature range of 500-600°C, EuS is oxidized to a mixture of Eu^{3+}-containing compounds (Eu_3S_4, Eu_2O_2S). In the range of 700–1000°C, a complete rearrangement of sulfide groups into sulfate occurs and the only europium sulfate $Eu_2O_2SO_4$ that is stable at these temperatures is formed. A diagram of changes in the chemical composition is constructed, showing the dependence of the composition of the reaction products on the temperature and time of the oxidation process. The structure refinement for $Eu_2O_2SO_4$ was performed by Rietveld method and two possible structures were considered: monoclinic with *C*2/*c* space group and orthorhombic with *I*222 space group. The results of a group theoretical analysis shows that experimental Infrared spectrum is compatible only with monoclinic structure.The luminescence intensity of europium oxysulfate $Eu_2O_2SO_4$ with characteristic 4f-4f transitions from the $^5D_0$ state was established as a function of

oxidation temperature. A spectral technique has been developed that makes it possible to detect an admixture of $Eu_2(SO_4)_3$ in the samples annealed at low temperatures (700°C).

Keywords: sulfur-containing europium compounds, high-temperature oxidation, thermal analysis, X-ray diffraction, crystal structure, photoluminescence

1. Introduction

Oxygen-containing compounds of europium Eu^{3+} attracted long attention of researchers due to the effective red luminescence, which has found application in many optical systems [1-9]. In recent years, a number of studies was implemented on the synthesis of compounds with stoichiometric europium content. The stoichiometry of the samples ensures the precise determination of the crystallographic positions of the radiating ions , and as a result, it becomes possible to establish the influence of the coordination environment on the luminescent properties of the Eu^{3+} ions [10–20]. Such self-activated phosphors are characterized by an almost complete absence of defects in the crystal structure. A qualitative description of the crystal structure of the material allows to track the influence of non-structural factors (synthesis temperature and time, particle size, etc.) on the luminescent-spectral properties.

Rare-earth oxidesulfates $Ln_2O_2SO_4$ exhibit a set of rather interesting magnetic properties [21-25]. The presence in oxysulfates of sulfur as a redox center determines their potential use as catalysts for the conversion process of water gas [26,27], solid oxide fuel cells and batteries [28,29], materials for storing gaseous oxygen [30-32]. Doped oxysulfates $(Ln_{1-x}Eu_x)_2O_2SO_4$ are promising for use as highly efficient phosphors when excited by ultraviolet light or X-rays. The compounds enhanced thermal stability and effective, reproducible luminescence characteristics [33-41]. However, to our best knowledge, data on the structural and spectroscopic properties of stoichiometric europium oxysulfate $Eu_2O_2SO_4$ are absent in the literature.

As it is well known, thermal destruction methods are convenient for obtaining materials with different properties [42-49]. In the synthesis of compounds containing isolated sulfate groups $(SO_4)^{2-}$, the methods applied for the oxidation of compounds containing sulfur in the lowest oxidation state S^{2-} are of particular attention. According to the data of [50], monosulfides of rare-earth elements are oxidized by air oxygen to oxysulfides Ln_2O_2S. Above this, various oxides Ln_xO_y appear as by-products of oxidation. According to the data reported in [52–56], the oxysulfides Ln_2O_2S are unstable in the air at high temperatures and the stoichiometric oxysulfates $Ln_2O_2SO_4$ are formed in this temperature range as the final reaction products. Comparatively, the alkaline earth compounds MeS (Me = Ca, Sr, Ba) are oxidized with atmospheric oxygen to stoichiometric sulphates $MeSO_4$ [57-59]. The inconsistency of the data suggests that europium monosulfide EuS can be oxidized with atmospheric oxygen to stoichimetric sulfates, and the method can be used for controlled synthesis of phosphors. Europium monosulfide can be obtained in the form of nanoparticles of different shapes (nanocubes, nanowires, nanofibres, etc.), and it can be used as a precursor in the synthesis of nanoparticles of oxygen-containing Eu^{3+} compounds. Respectively, it is important to study the mechanism of thermochemical transformations of europium monosulfide in the oxidizing atmosphere of air and the possibility of targeted production of oxygen-containing Eu^{3+} compounds in this process. Thus, the present study is aimed at the exploration of oxidation process of EuS in the air, including structural and spectroscopic analysis of the reaction products.

2. Materials and methods

2a. Syhtnesis

Europium monosulfide was synthesized from europium oxide Eu_2O_3 (ultrapure, 99.999%, TDM-72, Russia) in the reaction of high-temperature interaction with carbon disulfide CS_2 vapor (99.9%, Aldrich, France). According to X-ray diffraction (XRD) results, the Eu_2O_3 reagent does not contain foreign crystalline admixtures (Fig S1.a) and it crystallizes in cubic symmetry with cell

parameters listed in Table S1. The atomic coordinates and anisotropic thermal parameters (Table S2) are consistent with the literature data [60]. According to scanning electron microscopy (SEM) data, europium oxide powder is formed by faceted particles with average sizes of 1-10 μm (Fig. S1.b). Argon (99.99999%, Sibtechnology, Russia) was used as the carrier gas. The experimental set up used for the synthesis of EuS is shown in Figure S2. The carrier gas, at a rate of 6 l/h, was passed through carbon disulfide heated to 40°C. First, the argon flow carried CS_2 vapor was passed through a vertical quartz reactor with europium oxide charge (m = 10 g) at room temperature for 30 min. Then, using a programmable regulator, the temperature in the vertical furnace was increased to 1100°C at a rate of 50 °C/min. After that, the process was carried out at specified parameters for 5 h. The gases leaving the reactor, in order to absorb toxic components, were alternately passed through saturated aqueous solutions of copper sulfate and sodium hydroxide. After the synthesis stage, the reactor was cooled in the off-furnace mode to room temperature. Then, the heating of carbon disulfide was switched off, but argon flow was passed through the entire system for additional 1 h. When reactor is heated, the occurring process can be described by the equation:

$$2Eu_2O_3 + 3CS_2 \rightarrow 4EuS + 3CO_2 + 2S \quad (1)$$

The polycrystalline product obtained in this way is described by the EuS stoichimetric composition and does not contain any impurities. According to the data of SEM analysis, the powder is formed by uncut particles with sizes in the range of 1-5 μm and, in the particle shapes, a cubic motif can be observed. As it appears, the loss of faceting occurs due to nature of the anion exchange reaction governed by continuous diffusion mass transfer in the solid phase.

To evaluate the oxidation of europium monosulfide by atmospheric oxygen in isothermal mode, each charge of 0.5g EuS was evenly distributed as a thin layer in a flat ceramic boat with bottom 3×5 cm^2 in size. Then, all boats in parallel were gently inserted to the horizontal furnace and sample treatment was carried out in the air. When boat was removed from the furnace, it was cooled to room temperature in a desiccator with silica gel. The study of the phase composition of the

obtained oxidized samples was performed by XRD analysis. The experiments were conducted at 400, 500, 600, 700, 800, 900 and 1000 °C. The total time of oxidation at each temperature did not exceed 10 h. The samples for XRD analysis were taken from the furnace one by one with time inteval of 1 h. For high temperatures (800-1000°C), at the initial stages of oxidation, the samples were taken after 5, 10, 15 and 30 min. Totally, a set of 56 samples was obtained and analyzed.

2b. Methods of physical-chemical analysis

Thermal analysis in synthetic air (80% Ar-20% O_2) flow was carried out at a Simultaneous Thermal Analysis (STA) equipment 499 F5 Jupiter NETZSCH (Germany). The powder samples were inserted into alumina crucibles. The heating rate was 3°C/min. For enthalpy determination, the equipment was calibrated with use of standard metal substances, such as In, Sn, Bi, Zn, Al, Ag, Au, Ni. The heat effect peaks were determined with package «Proteus 6 2012». The peak temperature and area in parallel experiments were reproduced with inaccuracy lower than 3%.

X-ray phase analysis (XRD) was performed on a BRUKER D2 PHASER diffractometer with a linear detector LYNXEYE (CuKα radiation, Ni-filter). Rietveld refinement of all six samples was performed using package TOPAS 4.2 [61]. Almost all peaks were indexed by EuS, Eu_3S_4, Eu_2O_2S, $Eu_2O_2SO_4$ or $Eu_2(SO_4)_3$ phases. The powder diffraction data of $Eu_2O_2SO_4$ for Rietveld analysis were collected at room temperature with a Bruker D8 ADVANCE powder diffractometer (Cu-Kα radiation) and linear VANTEC detector. The step size of 2θ was 0.016° and the counting time was 5 s per step. Electron-microscopy analysis was carried out on an electron microscope JEOL JSM-6510LV. X-ray energy-dispersive analyzer was used to register X-rays at element spectrum plotting in selected sample surface areas. The inaccuracy in element content determination was equal to ±0.2%.

Fourier-transform infrared spectroscopy (FTIR) was carried out at a Fourier Transform Infrared Spectrometer FSM 1201. The sample for the investigation was prepared in the tablet form with addition of annealed KBr. The luminescence spectra at room temperature were recorded using a Horiba-Jobin-Yvon T64000 spectrometer. Spectral resolution of the measurement channel of the spectrometer was 2.7 cm^{-1}. The excitation radiation was the 514.5 nm line of Spectra Physics Stabilite 2017 laser. The exciting radiation does not fall into exact resonance with any of Eu^{3+} energy levels, however, off-resonance excitation is found to be quite enough in recording the luminescence spectra with high count rate. High resolution and extreme stability of excitation source were favorable for obtaining high quality luminescence spectra, as was shown in numerous similar studies [10,12,15].

3. Results and discussion

3a. Dynamic oxidation of EuS

Differential-thermal analysis of europium monosulfide in an atmosphere of synthetic air shows that the oxidation of EuS occurs over a wide temperature range, as shown in Fig. 1. Up to 500°C, there are no changes in the TG and DTA curves. Starting from 500°C, the increase in mass of the sample and a slight heat release are recorded. A plateau appears on the DTA curve in the temperature range of 700-800°C, which indicates a uniform flow of the process in this temperature range. Starting at 830°C, a powerful heat release is fixed on the DTA curve. The maximum of the thermal effect is at 875°C. The oxidation process is completed at 970°C: the TG curve goes to the plateau, the DTA curve comes to steady state. The mass gain at the process end corresponds to the formation of europium oxysulfate $Eu_2O_2SO_4$ by the reaction:

$$2EuS + 4O_2 \rightarrow Eu_2O_2SO_4 + SO_2 \quad (2)$$

However, the nature of the DTA curve does not allow describing the reaction as a one-stage process. Obviously, the processes occurring in the temperature ranges of 500-800°C and 800-1000°C correspond to different chemical reactions. Having data on enthalpies of formation of all compounds which formation can be assumed in the oxidation process [45, 62, 63], the enthalpy of the process was calculated by the equation:

$$2EuS_{(cub)} + 4O_{2(gas)} \rightarrow Eu_2O_2SO_{4(monocl)} + SO_{2(gas)} \quad (3)$$

The calculated enthalpy of the reaction $\Delta H^0_{calc} = -1731.1$ kJ/mol is in good relation to the experimentally determined value $\Delta H^0_{exp} = -1718.5$ kJ/mol.

3b. Isothermal oxidation

At 400°C, there are no changes in the qualitative phase composition of the samples for 10 h and all samples contain pure EuS (Figure 2.a). At 500°C, the samples principally change their phase composition. After 1 h interaction with air at this temperature, the sample contains a mixture of EuS, Eu_3S_4 and Eu_2O_2S. During the oxidation process for 10 h, the qualitative phase composition of the samples does not change, but the relative intensity of the reflexes of each phase changes, which indicates a variation in the phase percentage in the samples formed at 500°C (Figure 2.b). With a process time increase, the content of EuS gradually decreases and the content of the mixed sulfide Eu_3S_4 and oxysulfide Eu_2O_2S increases. It was not possible to reach complete oxidation of EuS to oxide reaction products even for 10 h.

However, carrying out the process at 600°C, it is possible to completely oxidize the EuS sample to reaction products Eu_3S_4 and Eu_2O_2S for 5 h (Fig. 2.c). Treating the EuS samples at this temperature up to 7 h does not lead to a change in the phase composition. But, after the treatment for 8 h, the impurity of europium (III) sulfate $Eu_2(SO_4)_3$ are detected (Fig. 2.d). The increase of the interaction time to 10 h results to an increase in the content of europium sulfate and oxysulfide in

samples and to a decrease in the content of mixed sulfide Eu_3S_4, which makes it possible to describe this process by the equation:

$$2Eu_3S_4 + 8O_2 \rightarrow 2Eu_2(SO_4)_3 + Eu_2O_2S + SO_2 \quad (4)$$

This change is characterized by the occurrence of a kinetically hindered oxidation of Eu_3S_4. Carrying out the process at 700°C allows to oxidize the sample to a mixture of mixed sulfide and europium oxysulfide Eu_2O_2S for 1 h interaction with air. Starting from the second hour of oxidation, europium oxysulfate $Eu_2O_2SO_4$ begins to appear in the samples (Figure 2.e). The rate of formation of oxysulfate is so great that, by the fifth hour and further, the samples are single-phase powders of $Eu_2O_2SO_4$.

At 800°C, after the five minutes processing, three phases are observed in the sample: Eu_3S_4, Eu_2O_2S, $Eu_2O_2SO_4$. An increase in the process time to 1 h leads to an increase in the europium oxysulfate content with a simultaneous decrease in the content of sulfides. A sample obtained after 2 h oxidation at 800°C and subsequent samples are single-phase europium oxysulfate $Eu_2O_2SO_4$ powders. After 5 min operation at 900°C, the sample contains a mixture of three phases: Eu_3S_4, Eu_2O_2S, $Eu_2O_2SO_4$ with an obvious predominance of oxysulfate component. After 15 min, all further samples are single-phase powders of europium oxysulfate. The samples obtained by oxidation of EuS at 1000°C for 5 min-10 h are single-phase powders of europium oxysulfate $Eu_2O_2SO_4$ (Figure 2.f).

According to electron microscopy, a tendency to loosening of the particles is observed during the decomposition process. The europium (II) sulfide is formed by grains ~1 μm in size (Figure 3.a). The particle cracks are weakly seen. Only in the shapes of some particles, cubic motif can be found. In the process of oxidation, the growth of nanocrystals of reaction products begins at the particle surfaces. Respectively, the particle destruction is evident. The temperature increase induces complete damage of the particles and the formation of samples consisting predominantly of

the X-ray amorphous phase. However, at high temperatures (> 900°C), the trend for aggregation of particles and the formation of microparticles with a monoclinic motif becomes decisive (Fig. 3d).

According to SEM analysis, a tendency to particle destruction is observed during the chemical decomposition process. The europium (II) sulfide is formed by the grains with sizes nearly 1 μm (Figure 3.a). The cut of particles is weakly expressed. Only in the structure of some of them you can see the cubic motif. In the process of oxidation, the growth of nanocrystals of reaction products begins at the surface of the particles. The particles loosen and exfoliate (Figure 3.b). An increase in temperature leads to complete disintegration of the particles and the formation of samples consisting predominantly of the X-ray amorphous phase (Figure 3c). However, at high temperatures (> 900°C), the desire for aggregation of particles and the formation of microparticles with a monoclinic motif becomes decisive (Fig. 3d). In the process of oxidation of EuS under isothermal conditions, the samples of six different phase compositions were obtained. The dependence of the phase composition on the temperature/time conditions is presented in Fig. 4. The processes occurring in the temperature range of 500-600 ° C, are kinetically hindered. At 500 °C, it was impossible to completely oxidize EuS for 10 h and residual EuS was always detected in the samples.

At 600 °C, the EuS sample was completely oxidized for 5 h (to a mixture of Eu_3S_4 + Eu_2O_2S). Three hours after reaching the equilibrium state, at the same temperature, another clearly kinetically hindered process is initiated: the oxidation of the mixed europium sulfide Eu_3S_4 with the formation of europium (III) sulfate $Eu_2(SO_4)_3$. In the system, at a given temperature (600°C), europium aspires to go completely into the trivalent state. Starting from 700°C, this kinetically hindered process is replaced by the process of combined oxidation of mixed sulfide and oxysulfide to oxysulfate. This process is completed for 5 h. With a further increase in temperature, the oxidation proceeds only according to this scheme, but the stages change one another much more quickly. Thus, the oxidation of EuS is a two-stage process: $EuS \rightarrow Eu_3S_4 + Eu_2O_2S \rightarrow Eu_2O_2SO_4$. According to DTA, in the second stage, the oxidation of two intermediate compounds proceeds in

parallel. However, it can be assumed that Eu_3S_4 containing europium in its divalent state enters this process first.

3c. Structural and spectroscopic properties of $Eu_2O_2SO_4$

One of the main oxidation products of europium monosulfide is oxysulfate $Eu_2O_2SO_4$. However, the correct diffraction identification of this product is rather difficult. The structure refinement for $Eu_2O_2SO_4$ was performed by Rietveld method. The recorded XRD pattern is shown in Figure 5. Almost all peaks can be indexed by monoclinic cell (*C*2/*c*) with parameters close to $Eu_2O_2SO_4$ [64] or by higher symmetry orthorhombic cell (*I*222) with parameters close to $Nd_2O_2SO_4$ [65]. Therefore, these two structure models were tested for the Rietveld refinements. Site of Nd ion was replaced by Eu. The refinements were stable and gave low *R*-factors (Table 1, Figure 5). Coordinates of atoms and main bond lengths are given in Tables S5 and S6, respectively. Both refined models were tested in checkCIF internet tool (https://checkcif.iucr.org/) and no serious problems (Alert A or Alert B types) were detected with the structures. Also, the difference plots are adequate for both cases, in spite of much better quality of the difference plot observed in *C*2/*c* model. The *I*222 model is of higher symmetry than the *C*2/*c* model; in addition, the *I*222 model has twice smaller cell volume and twice smaller number of refined parameters than the *C*2/*c* model (Fig. 6). However, the best fit with evidently smaller R-factor was obtained within the *C*2/*c* model. In this situation, choosing of correct model becomes a challenge. This was a reason why it was decided to make IR calculations for the structures obtained in both models.

Free tetrahedral SO_4^{2-} ion with T_d symmetry exhibits four internal vibrations. All four vibrations are Raman-active, whereas only ν_3 and ν_4 are infrared-active. In the solid state, ν_3 and ν_4 may split into two or three bands because of the site effect [66]. In Table 2, the correlation is given between the free SO_4^{2-} ion vibrations in T_d symmetry and the SO_4 internal vibrations in the case of monoclinic (*C*2/*c*) and orthorhombic (*I*222) cells in $Eu_2O_2SO_4$. The vibrational irreducible representations for the monoclinic structure at the center of the Brillouin zone is $\Gamma_{vibr} = 13A_g + 13A_u$

+ $14B_g$ + $14B_u$, where A_u + $2B_u$ are acoustic modes, $13A_g$ + $14B_g$ are Raman-active, while $12A_u$ + $12B_u$ modes are active in IR spectra. In the case of orthorhombic structure, the vibrational irreducible representations at the center of the Brillouin zone is $\Gamma_{vibr} = 5A + 6B_1 + 8B_2 + 8B_3$, where $B_1 + B_2 + B_3$ are acoustic modes, $5A + 5B_1 + 7B_2 + 7B_3$ are Raman-active modes, while $5B_1 + 7B_2 + 7B_3$ modes are active in IR spectra.

From the correlation diagrams and vibrational irreducible representations, we can conclude that four spectral bands should be observed in the range of stretching vibrations of SO_4 tetrahedra in Raman spectra as in the case of monoclinic as in the case of orthorhombic structures. Infrared spectra of *C*2/*c* structure should contain four bands in this region while symmetric stretching *A* mode is forbidden in the case of orthorhombic structure and only three spectral bands should be observed. Thus, the recorded Infrared spectrum of $Eu_2O_2SO_4$, as shown in Figure 7, corresponds to the monoclinic *C*2/*c* structure.

Luminescence spectra of the $Eu_2O_2SO_4$ samples fabricated at different annealing temperatures (700, 800, 900 and 1000°C) were recorded using excitation wavelength 514.5 nm with the spectral resolution 2.7 cm^{-1}. The samples were taken in approximately equal quantities in order to enable qualitative comparison of luminescent intensities between them. All spectra are similar at the first glance, containing characteristic luminescent bands of Eu^{3+} ion at the transitions $^5D_0 \rightarrow {}^7F_J$ (J = 0-4) [10,12,67]. Transitions with J=5,6 were also observed but their intensity was too small to be depicted in Fig. 8. Among four recorded spectra, the three ones taken from samples oxidized at higher temperatures (from 800 to 1000°C) exhibit almost identical shape of intraband crystal field splitting while the intensity of luminescence grows with the oxidation temperature increase. The most pronounced intensity growth can be observed for the sample oxidized at 900°C in comparison to that oxidized at 800°C (2.8 times maximum peaks intensities). This intensity behavior is typical for annealing of different crystalline phosphors and is commonly treated as the effect of better crystallinity reached at higher temperatures.

The luminescence spectrum of the sample oxidized at 700°C shows certain differences in band shapes with respect to the samples obtained at higher temperatures. First of all, the region of ultranarrow transition $^5D_0 \rightarrow {}^7F_0$ contains two peaks, as can be seen in Fig. S4. Fig. S4 presents untranarrow lines in the samples annealed at 700 and 800 C as well as the same line in recently studied $Eu_2(SO_4)_3$ [12]. The latter spectrum is featured by the ultranarrow line position coinciding with one of the peaks in the spectrum of the sample annealed at 700°C, while the sample annealed at 800°C contains a single ultranarrow line coinciding with the more intense component in the spectrum of the sample annealed at 700°C. Therefore, ultranarrow line at 579,6 nm must be ascribed to $Eu_2O_2SO_4$ in both samples under study, while ultranarrow component at 579.0 nm in the sample annealed at 700°C must be ascribed to the admixture of $Eu_2(SO_4)_3$. Curiously, the ultranarrow line in admixture $Eu_2(SO_4)_3$ is almost completely symmetric, evidencing its good crystalline quality, in comparison with asymmetric line in pure $Eu_2(SO_4)_3$ [12]. The presence of $Eu_2(SO_4)_3$ admixture in the sample annealed at 700°C also influences the rest of the luminescent bands of it, as illustrated by Fig. S5, where comparison of this sample spectrum with that of 800 C sample is presented. However, subtraction of 800°C sample spectrum multiplied by adjustable factor being 0.78 in our case, from 700°C sample spectrum results in the spectrum well coinciding with that of $Eu_2(SO_4)_3$ (Fig.S6). Therefore, the sample annealed at 700°C is likely to contain 78% of $Eu_2O_2SO_4$ and 22% of $Eu_2(SO_4)_3$.

The formation of europium sulfate occurs in accordance with equation 4. The absence of spectral lines of europium oxysulfide is due to its instability at given temperatures and vice versa according to the equation:

$$Eu_2O_2S + 2O_2 \rightarrow Eu_2O_2SO_4 \quad (5)$$

It was not possible to detect the impurity $Eu_2(SO_4)_3$ by X-ray diffraction analysis due to the low crystallinity of the samples.

4. Conclusions

Thus, in the present study, the process of high-temperature oxidation of EuS with atmospheric oxygen, in dynamic and isothermal modes, has been observed. It is established that oxidation proceeds in two stages and is associated with several topochemical processes of varying degrees of complexity. The applicability of EuS oxidation as a method for the synthesis of europium oxysulfate $Eu_2O_2SO_4$ is established. According to the data of luminescence spectroscopy, the synthesis temperature has a significant effect on the luminescence intensity in the $Eu_2O_2SO_4$ samples, in view of different crystallinity degree. It was clearly established that structural analysis of a compound $Eu_2O_2SO_4$ is possible only by combining diffraction and spectral methods.The future works can be targeted at the synthesis of catalytically active powders of $Eu_2O_2SO_4$ in a nanostructure by the oxidation of EuS nanopowders.

Acknowledgements

The authors are grateful for the support from RFBR (16-02-00102, 16-52-48010, 17-52-53031, 18-02-00754, 18-08-00985 and 18-32-20011).

References

1. Shuxing Li, Le Wang, Daiming Tang, Yujin Cho, Xuejian Liu, Xingtai Zhou, Lu Lu, Lin Zhang, Takashi Takeda, Naoto Hirosaki, Rong-Jun Xie, Achieving High Quantum Efficiency Narrow-Band β-Sialon: Eu^{2+} Phosphors for High-Brightness LCD Backlights by Reducing the Eu^{3+} Luminescence Killer, Chem. Mater. 30 (2) (2017) 494-505.

2. Xiaofei Shi, Zhihao Wang, Toshiaki Takei, Xuejiao Wang, Qi Zhu, Xiaodong Li, Byung-Nam Kim, Xudong Sun, Ji-Guang Li, Selective Crystallization of Four Tungstates ($La_2W_3O_{12}$,

$La_2W_2O_9$, $La_{14}W_8O_{45}$, and $La_6W_2O_{15}$) via Hydrothermal Reaction and Comparative Study of Eu^{3+} Luminescence, Inorg. Chem. 57 (11) (2018) 6632-6640.

3. Chunling Li, Xueling Fan, Peng Jiang, Xiaochao Jin, Delamination-indicating of atmosphere-plasma-sprayed thermal barrier coating system using Eu^{3+} luminescence mapping, Mater. Lett. 222 (2018) 41-44.

4. F. Baur, T. Jüstel, Uranyl sensitized Eu^{3+} luminescence in $Ln(UO_2)_3(PO_4)_2O(OH)\cdot 6H_2O$ phosphors (Ln= Y, Eu, La) for warm-white light emitting diodes, J. Lum. 196 (2018) 431-436.

5. M. Behrendt, S. Mahlik, M. Grinberg, D. Stefanska, P.J. Deren, Influence of charge transfer state on Eu^{3+} luminescence in $LaAlO_3$, by high pressure spectroscopy, Opt. Mater. 63 (2017) 158-166.

6. M.Puchalska, High enhancement of Eu^{3+} luminescence in $SrAl_4O_7$ phosphor by means of charge compensation with Na^+ ions, Opt. Mater. 72 (2017) 452-458.

7. M.A. van de Haar, J. Werner, N. Kratz, T. Hilgerink, M. Tachikirt, J. Honold, M.R. Kramers, Increasing the effective absorption of Eu^{3+}-doped luminescent materials towards practical light emitting diodes for illumination applications, App. Phys. Lett. 112 (13) (2018) 132101.

8. R. Laishram, U. Maitra, Bile Salt- Derived Eu^{3+} Organogel and Hydrogel: Water- Enhanced Luminescence of Eu^{3+} in a Gel Matrix, Chem. Select. 3 (2) (2018) 519-523.

9. Pinglu Shi, Zhiguo Xia, Maxim S. Molokeev, Victor V. Atuchin, Crystal chemistry and luminescence properties of red-emitting $CsGd_{1-x}Eu_x(MoO_4)_2$ solid-solution phosphors, Dalton Trans. 43 (25) (2014) 9669-9676.

10. V.V. Atuchin, A.S. Aleksandrovsky, O.D. Chimitova, T.A. Gavrilova, A.S. Krylov, M.S. Molokeev, A.S. Oreshonkov, B.G. Bazarov, J.G. Bazarova, Synthesis and spectroscopic properties of monoclinic α-$Eu_2(MoO_4)_3$, J. Phys. Chem. C 118 (28) (2014). 15404-15411.

11. Haipeng Ji, Zhaohui Huang, Zhiguo Xia, Maxim S. Molokeev, Xingxing Jang, Zheshuai Lin, Victor V. Atuchin, Comparative investigations of the crystal structure and photoluminescence property of eulytite-type $Ba_3Eu(PO_4)_3$ and $Sr_3Eu(PO_4)_3$, Dalton Trans. 44 (16) (2015) 7679-7686.

12. Yu.G. Denisenko, A.S. Aleksandrovsky, V.V. Atuchin, A.S. Krylov, M.S. Molokeev, A.S. Oreshonkov, N.P. Shestakov, O.V. Andreev, Exploration of structural, thermal and spectroscopic properties of self-activated sulfate $Eu_2(SO_4)_3$ with isolated SO_4 groups, J. Indust. Eng. Chem. 68 (2018) 109-116.

13. A.H. Reshak, Z.A. Alahmed, J. Bila, V.V. Atuchin, B.G. Bazarov, O.D. Chimitova, M.S. Molokeev, I.P. Prosvirin, A.P. Yelisseyev, Exploration of the electronic structure of monoclinic α-$Eu_2(MoO_4)_3$: DFT-based study and X-ray photoelectron spectroscopy, J. Phys. Chem. C. 120 (19) (2016) 10559-10568.

14. Xuejiao Wang, Maxim S. Molokeev, Qi Zhu, Ji-Guang Li, Controlled hydrothermal crystallization of anhydrous $Ln_2(OH)_4SO_4$ (Ln = Eu-Lu, Y) as a new family of layered rare earth matel hydrooxides, Chem. Europ. J. 23 (2017) 16034-16043.

15. V.V. Atuchin, A.K. Subanakov, A.S. Aleksandrovsky, B.G. Bazarov, J.G. Bazarova, T.A. Gavrilova, A.S. Krulov, M.S. Molokeev, A.S. Oreshonkov, S.Yu. Stefanovich, Structural and spectroscopic properties of noncentrosymmetric self-activated borate $Rb_3EuB_6O_{12}$ with B_5O_{10} units, Mater. Des. 140 (2018) 488-494.

16. Myung Ho Choi, Min Kyung Kim, Vin Na Jo, Dong Woo Lee, II Wun Shim, Kang Min Ok, Hydrothermal Syntheses, Structures, and Characterizations of Two Lanthanide Sulfate Hydrates Materials, $La_2(SO_4)_3 \cdot H_2O$ and $Eu_2(SO_4)_3 \cdot 4H_2O$, Bull. Korean Chem. Soc. 31 (4) (2010) 1077-1080.

17. L. Paama, I. Pitkanen, J. Valkonen, E. Parnoja, H. Kola, P. Peramaki, Thermal and spectroscopic investigation of europium and samarium sulphates hydrates by TG-FTIR and ICP-MS techniques, Talanta 67 (5) (2005) 897-902.

18. Yan Xu, Shaohua Ding, Xuefang Zheng. Hydrothermal synthesis, crystal structure and properties of 2-D and 3-D lanthanide sulfates, J. Sol. State Chem. 180 (7) (2007) 2020-2025.

19. Yu.G. Denisenko, V.V. Atuchin, M.S. Molokeev, A.S. Aleksandrovsky, A.S. Krylov, A.S. Oreshonkov, S.S. Volkova, O.V. Andreev, Structure, thermal stability, and spectroscopic properties of triclinic double sulfate $AgEu(SO_4)_2$ with isolated SO_4 Groups, Inorg. Chem. 57 (21) (2018). 13279-13288.

20. X. Zhang, Yu. Ma, H. Zhao, C. Jiang, Yu. Sun, Ya. Xu, Synthesis, characterization and very strong luminescence of a new 3D europium sulfate $Eu_2(H_2O)_4(SO_4)_3$, J. Struct. Chem. 52 (5) (2011) 954-958.

21. Fashen Chen, Gen Chen, Tao Liu, Ning Zhang, Xiaohe Liu, Hongmei Luo, Junhui Li, Limiao Chen, Renzhi Ma, Guanzhou Qiu, Controllable fabrication and optical properties of uniform gadolinium oxysulfate hollow spheres, Sci. Reports 5 (2015) 17934.

22. M. Shaterian, M.A. Rezvani, V. Shahsavandi, K. Qasemi, Synthesis, characterization and electrochemical properties of lanthanum oxysulfate nanoceramic, J. Nanostruct. 7 (2) (2017) 97-102.

23. Danyang Ma, Chungen Li, Lei Wang, Hao Liu, Shengliang Zhong, Yuan Li, Preparation of $RE_2O_2SO_4$ (RE= La, Pr-Lu) microspheres from rare-earth-based infinite coordination polymers, J. Nanoparticle Res. 19 (10) (2017) 341.

24. W. Paul, Magnetism and magnetic phase diagram of $Gd_2O_2SO_4$ I. Experiments, J. Magn. Magn. Mater. 87 (1990) 23-28.

25. Jinbao Lian, Xudong Sun, Xiaodong Li, Synthesis, characterization and photoluminescence properties of $(Gd_{1-x},Eu_x)_2O_2SO_4$ sub-microphosphors by homogeneous precipitation method, Mater. Chem. Phys. 125 (2011). 479-484.

26. I. Valsamakis, M. Flytzani-Stephanopoulos, Sulfur-tolerant lanthanide oxysulfide catalysts for the high-temperature water–gas shift reaction, Appl. Cat.. B: Environ. 106 (2011) 255-263.

27. S. Tan, S.N. Paglieri, D. Li, Nano-scale sulfur-tolerant lanthanide oxysulfide/oxysulfate catalysts for water–gas-shift reaction in a novel reactor configuration, Cat. Comm. 73 (2016) 16-21.

28. F.J.A. Loureiro, T. Yang, D.G. Stroppa, D.P. Fagg, $Pr_2O_2SO_4$–$La_{0.6}Sr_{0.4}Co_{0.2}Fe_{0.8}O_{3-\delta}$: a new category of composite cathode for intermediate temperature-solid oxide fuel cells, J. Mater. Chem. A. 3 (24) (2015) 12636-12641.

29. P.V.M. Dixini, V.G. Celante, M.F.F. Lelis, M.B.J.G. Freitas, Recycling of the anode from spent Ni-MH batteries for synthesis of the lanthanide oxysulfide/oxysulfate compounds used in an oxygen storage and release system, J. Power Sources. 260 (2014) 163-168.

30. W. Zhang, I.W.C.E. Arends, K. Djanashvili, Nanoparticles of lanthanide oxysulfate/oxysulfide for improved oxygen storage/release, Dalton Trans. 45 (36) (2016) 14019-14022.

31. Keita Ikeue, Tomoatsu Kawano, Masakazu Eto, Dongjie Zhang, Masato Machida, X-ray structural study on the different redox behavior of La and Pr oxysulfates/oxysulfides, J. Alloys Compd. 451 (1-2) (2008) 338-340.

32. Dongjie Zhang, Takahiro Kawada, Fumihiko Yoshioka, Masato Machida, Oxygen Gateway Effect of $CeO_2/La_2O_2SO_4$ Composite Oxygen Storage Materials, ACS Omega 1 (5) (2016) 789-798.

33. S. Kim, T. Masui, N. Imanaka, Synthesis of red-emitting phosphors based on gadolinium oxysulfate by a flux method, Electrochemistry 77 (8) (2009) 611-613.

34. Fan Liu, Jing Bao Lian, Guang Xi Xu, Nian Chu Wu, A Facile Co-Precipitation Synthesis and Luminescence Properties of Red-Emitting $La_2O_2SO_4$:x%Eu^{3+} Nanophosphors, Solid State Phenom. 281 (2018) 679-685.

35. Jingbao Lian, Fan Liu, Jing Zhang, Yanyu Yang, Xuri Wang, Zhaoren Zhang, Feng Liu, Template-free hydrothermal synthesis of $Gd_2O_2SO_4$:Eu^{3+} hollow spheres based on urea-ammonium sulfate (UAS) system, Optik 127 (20) (2016) 8621-8628.

36. Xing Li, Jingbao Lian, Synthesis and characterizations of pompon-like $Y_2O_2SO_4$:Eu^{3+} phosphors using a UBHP technique based on UAS system, Optik 127 (1) (2016) 401-406.

37. Jinbao Lian, Hua Qin, Ping Liang, Feng Liu, Co-precipitation synthesis of $Y_2O_2SO_4$:Eu^{3+} nanophosphor and comparison of photoluminescence properties with Y_2O_3:Eu^{3+} and Y_2O_2S:Eu^{3+} nanophosphors, Sol. State Sci. 48 (2015) 147-154.

38. Jingbao Lian, Feng Liu, Xuejiao Wang, Xudong Sun, Hydrothermal synthesis and photoluminescence properties of $Gd_2O_2SO_4$:Eu^{3+} spherical phosphor, Powder Techn. 253 (2014) 187-192.

39. Jingbao Lian, Ping Liang, Bingxin Wang, Feng Liu, Homogeneous precipitation synthesis and photoluminescence properties of $La_2O_2SO_4$:Eu^{3+} quasi-spherical phosphors, J. Ceram. Process. Res. 15 (2014) 382-388.

40. Guangxi Xu, Fan Liu, Jingbao Lian, Nianchu Wu, Xue Zhang, Jiao He, Synthesis and optical properties of Eu^{3+} ion-doped $La_2O_2S_2$ via a solid state reaction method using $La_2O_2SO_4$ as a raw material, Ceram. Int. 44 (15) (2018). 19070-19076.

41. O.V. Andreev, Yu.G. Denisenko, E.I. Sal'nikova, N.A. Khritokhin, K.S. Zyryanova, Specifics of reactions of cerium sulfate and europium sulfate with hydrogen, Russ. J. Inorg. Chem. 61 (3) (2016) 296-301.

42. O.V. Andrrev, I.A. Razumkova, A.N. Boiko. Synthesis and thermal stability of rare earth compounds REF_3, $REF_3 \cdot nH_2O$ and $(H_3O)RE_3F_{10} \cdot nH_2O$ (RE= Tb− Lu, Y), obtained from sulphide precursors, J. Fluor. Chem. 207 (2018) 77-83.

43. I.A. Razumkova, Synthesis of $NaYF_4$ compounds from sulfide precursors, J. Fluor. Chem. 205 (2018) 1-4.

44. Yu.G. Denisenko, N.A. Khritokhin, O.V. Andreev, S.A. Basova, E.I. Sal'nikova, A.A. Polkovnikov. Thermal decomposition of europium sulfates $Eu_2(SO_4)_3 \cdot 8H_2O$ and $EuSO_4$, J. Sol. State Chem. 255 (2017) 219-224.

45. H. Stark, R.L.N. Yatavelli, S.L. Thompson, H. Kang, J.E. Krechmer, J.R. Kimmel, B.B. Palm, W. Hu, P.L. Hayes, D.A. Day, P. Campuzano-Jost, M.R. Canagaranta, J.T. Jayne, D.R. Worsnop, J.L. Jimenes, Impact of thermal decomposition on thermal desorption instruments: advantage of thermogram analysis for quantifying volatility distributions of organic species, Environ. Sci. Technol. 51 (15) (2017) 8491-8500.

46. P. Povea, J.L. Arroyo, G. Carreno, A. Norambuena, P.L. Rios, M.B. Camarada, I. Chavez, J.M. Manriquez, C. Morales-Verdejo, Catalytic effects of p-phenylene-bridged methylated binuclear ferrocenes on thermal decomposition of the main component of composite solid propellants, Thermochim. Acta 666 (2018) 181-189.

47. X. Liu, K.A. Salmeia, D. Rentsch, J. Hao, S. Gaan, Thermal decomposition and flammability of rigid PU foams containing some DOPO derivatives and other phosphorus compounds, J. Anal. Appl. Pyrolysis 124 (2017) 219-229.

48. M. Unni, A.M. Uhl, S. Savliwala, B.H. Savitzky, R. Dhavalikar, N. Garraud, D.P. Arnold, L.F. Kourkoutis, J.S. Andrew, C. Rinaldi, Thermal decomposition synthesis of iron oxide nanoparticles with diminished magnetic dead layer by controlled addition of oxygen, ACS Nano. 11 (2) (2017) 2284-2303.

49. J.L. Jambor, D.K. Nordstrom, C.N. Alpers, Metal-sulfate salts from sulfide mineral oxidation, Rev Mineral. Geochem. 40 (1) (2000) 303-350.

50. Y.L. Suponitskii, G.M. Kuz'micheva, A.A. Eliseev, Lanthanide Oxide Sulphides, Russ. Chem. Rev. 57 (3) (1988) 209-220.

51. K. Ikeue, T. Kawano, D. Zhang, M. Eto, M. Machida Local Structure Analysis of Lanthanide Oxysulfate Having a Large-Capacity Oxygen Storage Property, Chemistry. 25 (B) (2007) 30.

52. W.H. Shen, S. Naito, Easy precipitation method for preparation of cerium added $La_2O_2SO_4$ used for oxygen storage, Adv. Mater. Res. 886 (2014) 196-199.

53. M. Miura, H. Hirata, K. Ishibashi, M. Machida, Study of Large OSC Materials ($Ln_2O_2SO_4$) on the Basis of Sulfur Redox Reaction, SAE Technical Paper. 2009-01-1071 (2009).

54. M. Machida, T. Kawano, M. Eto, D. Zhang, K. Ikeue, Ln dependence of the large-capacity oxygen storage/release property of Ln oxysulfate/oxysulfide systems, Chem. Mater. 19 (4) 2007 954-960.

55. M. Machida, K. Kawamura, K. Ito, K. Ikeue, Large-capacity oxygen storage by lanthanide oxysulfate/oxysulfide systems, Chem. Mater. 17 (6) (2005) 1487-1492.

56. R.A. Lidin, V.A. Molochko, L.L. Andreeva, Inorganic Chemistry in Reactions: a Handbook, Drofa, Moscow. (2007).

57. N.N. Greenwood, A. Earnshaw, Chemistry of the Elements. Elsevier, (2012).

58. Yu.D. Tret'yakov, L.I. Martynenko, A.N. Grigor'ev, A.Yu. Tsivadze, Inorganic Chemistry. Chemistry of the Elements: Textbook for Universities: Chemistry, Moscow. (2001).

59. Z.K. Heiba, Y. Akin, W. Sigmund, Y.S. Hascicek. X-ray structure and microstructure determination of the mixed sesquioxides $(Eu_{1-x}Yb_x)_2O_3$ prepared by a sol–gel process. J. Appl. Cryst. 36 (6) (2003) 1411-1416.

60. Bruker AXS TOPAS V4: General profile and structure analysis software for powder diffraction data. – User's Manual. Bruker AXS, Karlsruhe, Germany. 2008.

61. O.D. McMasters, K.A. Gschneidner, E. Kaldis, G. Sampietro, High-temperature enthalpies and standard Gibbs free energies of formation of the europium chalcogenides: EuO, EuS, EuSe, and EuTe, J. Chem. Thermod. 6 (9) (1974) 845-857.

62. J.R. Eckman, F.D. Rossini, The heat of formation of sulphur dioxide, Bureau of Standards Journal of Research, 3 (1929) 597-618.

63. I. Hartenbach, T. Schleid, Serendipitous Formation of Single- Crystalline $Eu_2O_2[SO_4]$, Z. Anorg. Allgem. Chem. 628 (9- 10) (2002) 2171-2171.

64. N.N. Golovnev, M.S. Molokeev, S.N. Vereshchagin, V.V. Atuchin, Synthesis and thermal transformation of a neodymium (III) complex $[Nd(HTBA)_2(C_2H_3O_2)(H_2O)_2]\cdot 2H_2O$ to noncentrosymmetric oxosulfate $Nd_2O_2SO_4$. J. Coord. Chem 68 (11) (2015) 1865-1877.

65. K. Nakamoto, Infrared and Raman Spectra of Inorganic and Coordination Compounds, 6th edn. Wiley, New York etc. (2009).

66. V.V . Atuchin, A.S. Aleksandrovsky, B.G. Bazarov, J.G. Bazarova, O.D. Chimitova, Yu.G. Denisenko, T.A. Gavrilova, A.S. Krylov, E.A. Maximovskiy, M.S. Molokeev, A.S. Oreshonkov, A.M. Pugachev, N.V. Surovtsev, Exploration of structural, vibrational and

spectroscopic properties of self-activated orthorhombic double molybdate $RbEu(MoO_4)_2$ with isolated MoO_4 units, J. Alloys Compd. 785 (2019) 692-697.

Captions

Fig. 1. DTA/TG of EuS in synthetic air

Fig. 2. Difference Rietveld plot of: a) EuS; b) EuS-Eu_3S_4-Eu_2O_2S; c) Eu_3S_4-Eu_2O_2S; d) Eu_3S_4-Eu_2O_2S-$Eu_2(SO_4)_3$; e) Eu_3S_4-Eu_2O_2S-$Eu_2O_2SO_4$; f) $Eu_2O_2SO_4$.

Fig. 3. The transformation of particles during the oxidation of europium monosulfide, depending on the process temperature: a) 25°C (EuS); b) 500°C (EuS-Eu_3S_4-Eu_2O_2S); c) 700°C (EuS-Eu_3S_4-Eu_2O_2S-$Eu_2O_2SO_4$); d) 800°C ($Eu_2O_2SO_4$)

Fig.4. Kinetic scheme of changes in the chemical composition of the samples during oxidation of europium monosulfide with air oxygen. Legend: 1-EuS; 2-EuS + Eu_3S_4 + Eu_2O_2S; 3-Eu_3S_4 + Eu_2O_2S; 4-Eu_3S_4 + Eu_2O_2S + $Eu_2(SO_4)_3$; 5-Eu_3S_4 + Eu_2O_2S + $Eu_2O_2SO_4$; 6-$Eu_2O_2SO_4$

Fig.5. Difference Rietveld plot of $Eu_2O_2SO_4$ by two different structural models: a) *C*2/*c*; b) *I*222.

Fig.6. Crystal structures of $Eu_2O_2SO_4$ in two different structural models *C*2/*c* and *I*222

Fig.7. Infrared spectra of $Eu_2O_2SO_4$.

Fig.8. The luminescence spectra of $Eu_2O_2SO_4$ samples obtained at different oxidation temperatures of europium sulfide are: a - 700 ° C, b - 800 ° C, c - 900 ° C, d - 1000 ° C

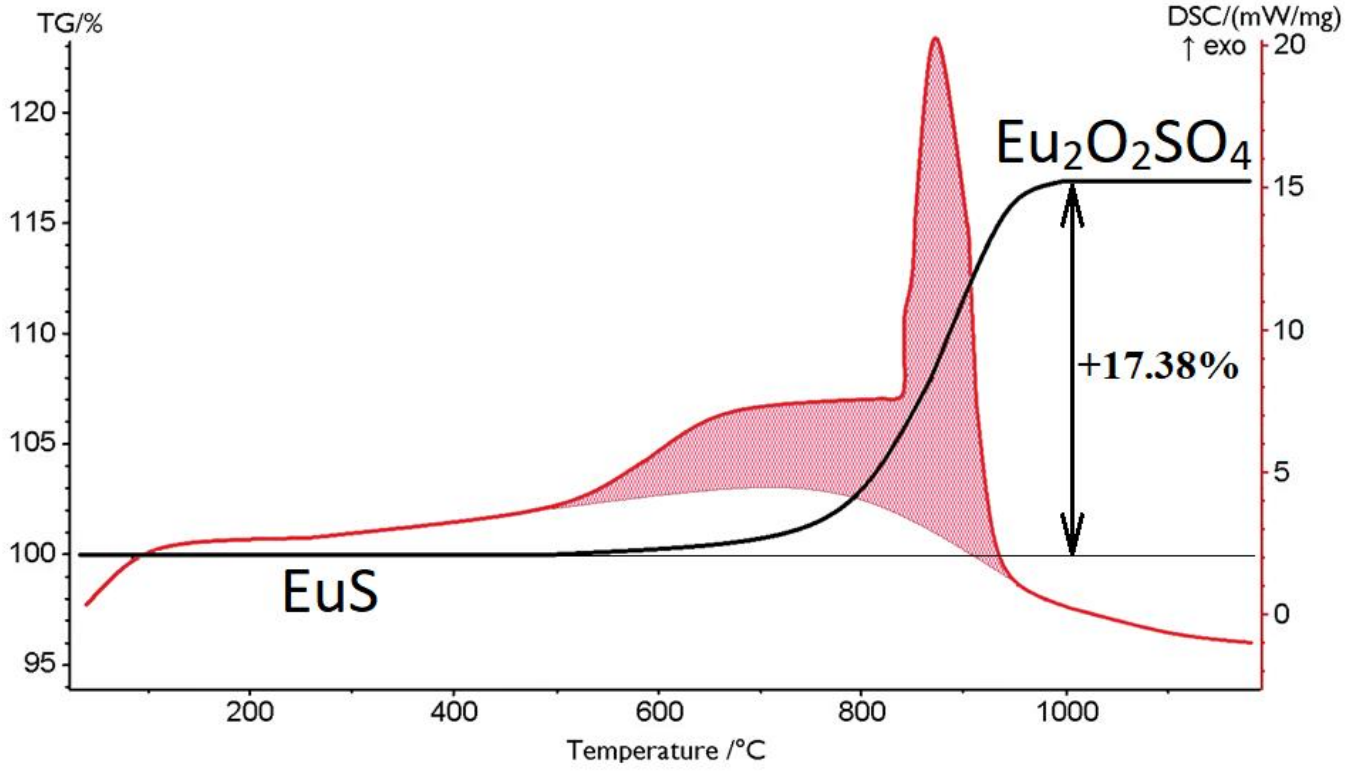
TG/%
DSC/(mW/mg)
↑ exo
120
115
110
105
100
95
20
15
10
5
0
Eu2O2SO4
+17.38%
EuS
200
400
600
800
1000
Temperature /°C

Fig.1.

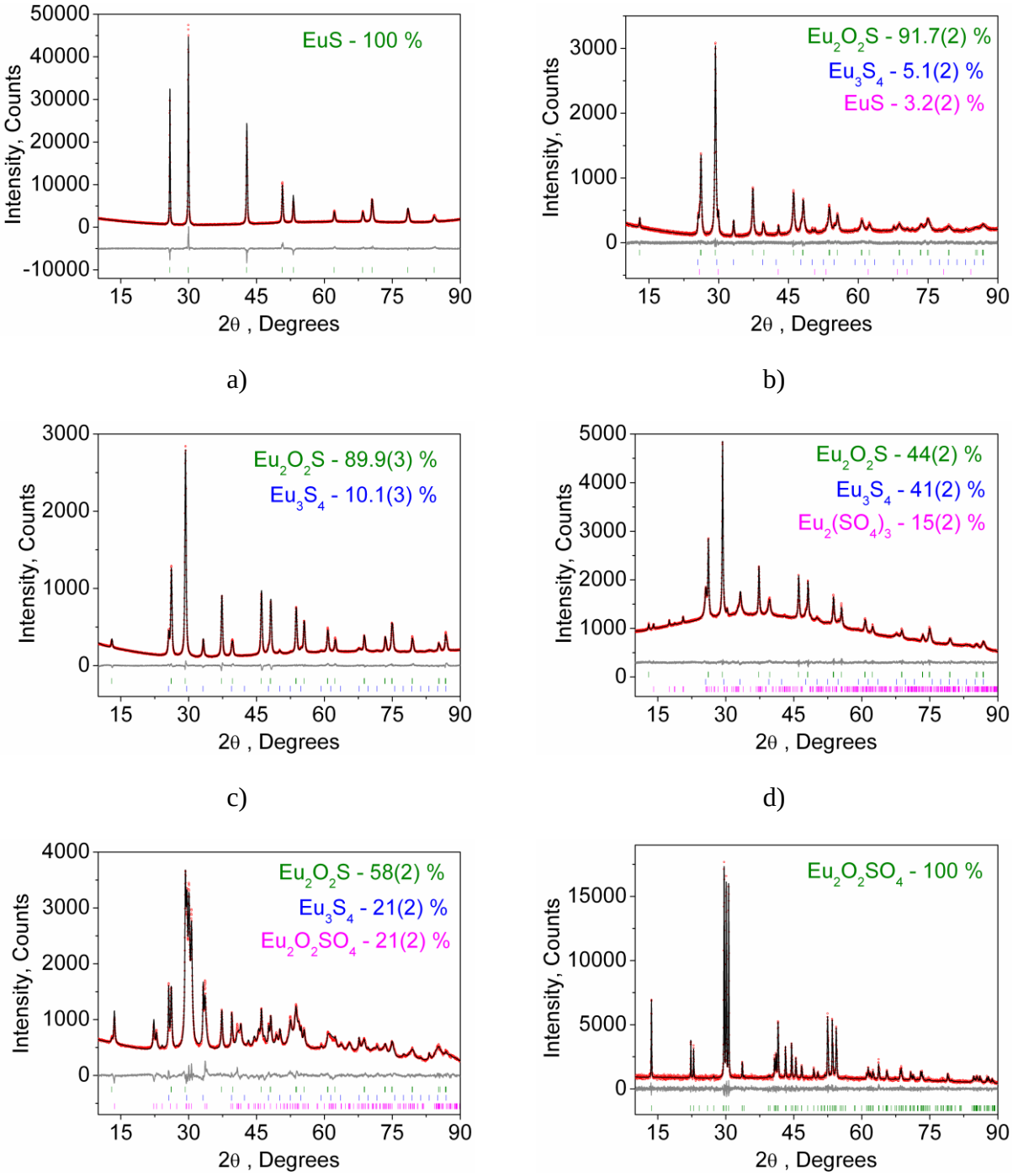
EuS - 100 %
Intensity, Counts
2θ , Degrees
a)
Eu2O2S - 91.7(2) %
Eu3S4 - 5.1(2) %
EuS - 3.2(2) %
Intensity, Counts
2θ , Degrees
b)
Eu2O2S - 89.9(3) %
Eu3S4 - 10.1(3) %
Intensity, Counts
2θ , Degrees
c)
Eu2O2S - 44(2) %
Eu3S4 - 41(2) %
Eu2(SO4)3 - 15(2) %
Intensity, Counts
2θ , Degrees
d)
Eu2O2S - 58(2) %
Eu3S4 - 21(2) %
Eu2O2SO4 - 21(2) %
Intensity, Counts
2θ , Degrees
e)
Eu2O2SO4 - 100 %
Intensity, Counts
2θ , Degrees
f)

Fig. 2.

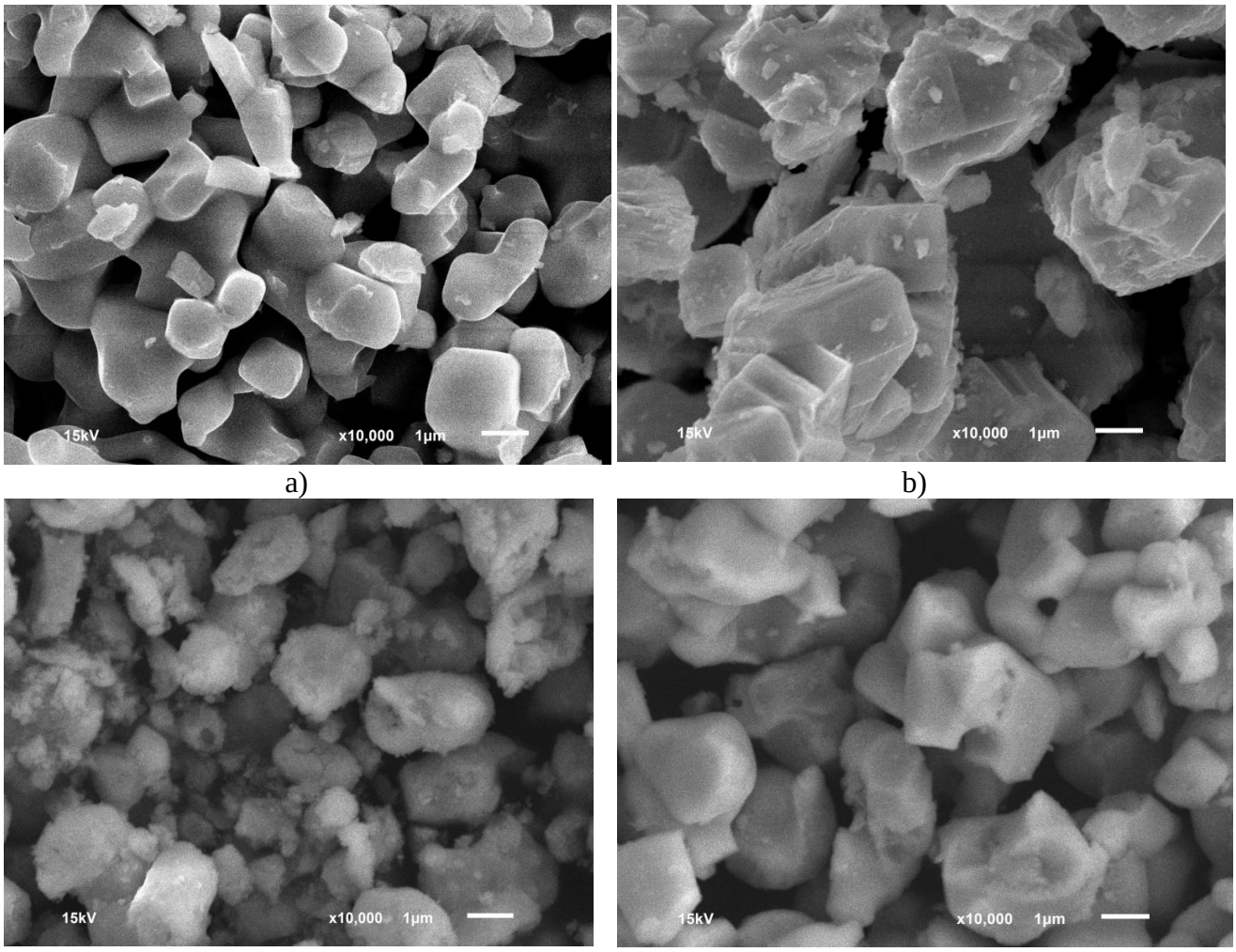
15kV
x10,000 1μm
15kV
x10,000 1μm
15kV
x10,000 1μm
15kV
x10,000 1μm

a) b)

c) d)

Fig. 3

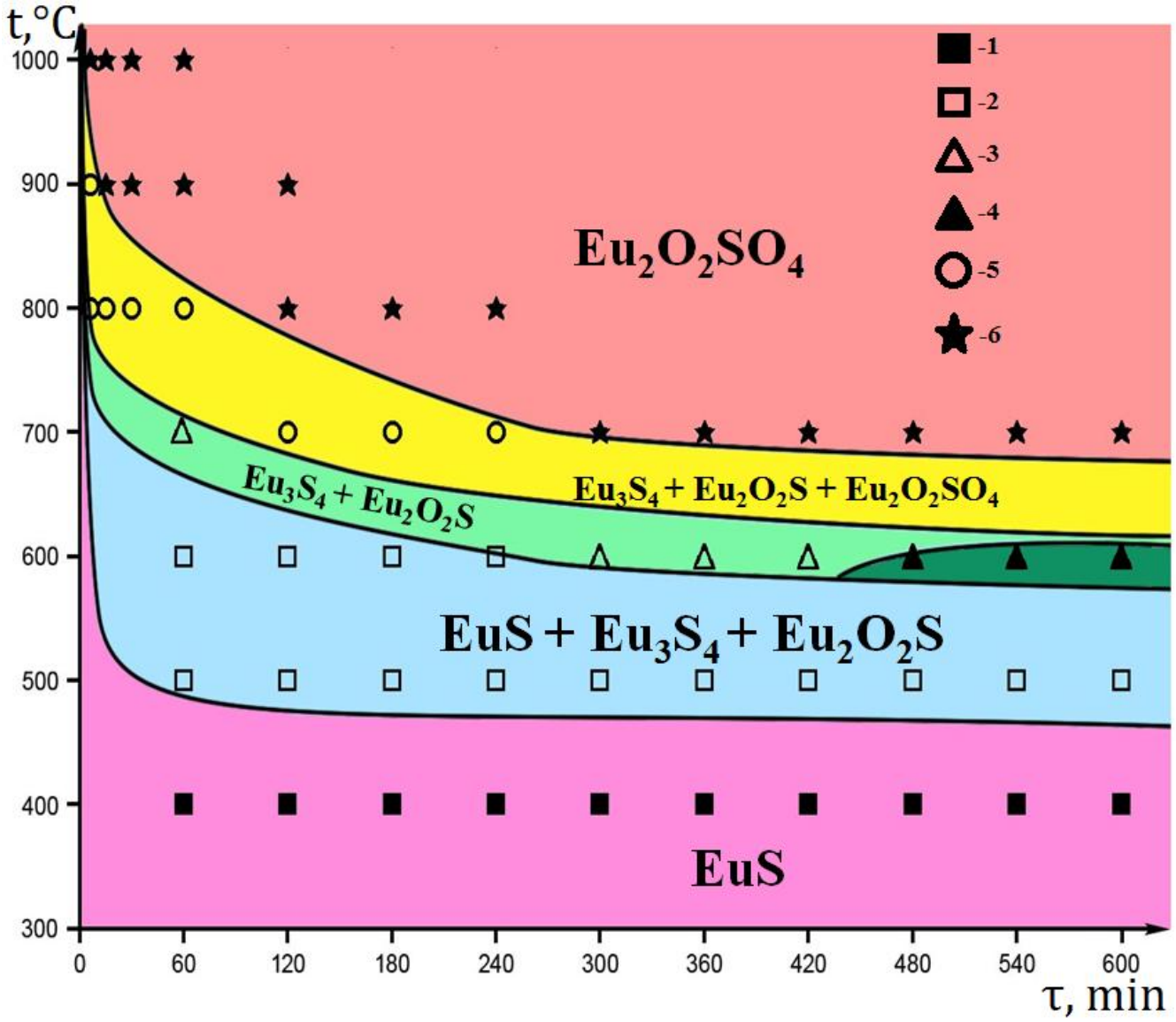
t,°C
1000
900
800
700
600
500
400
300
0
60
120
180
240
300
360
420
480
540
600
τ, min
-1
-2
-3
-4
-5
-6
Eu2O2SO4
Eu3S4 + Eu2O2S + Eu2O2SO4
Eu3S4 + Eu2O2S
EuS + Eu3S4 + Eu2O2S
EuS

Fig. 4

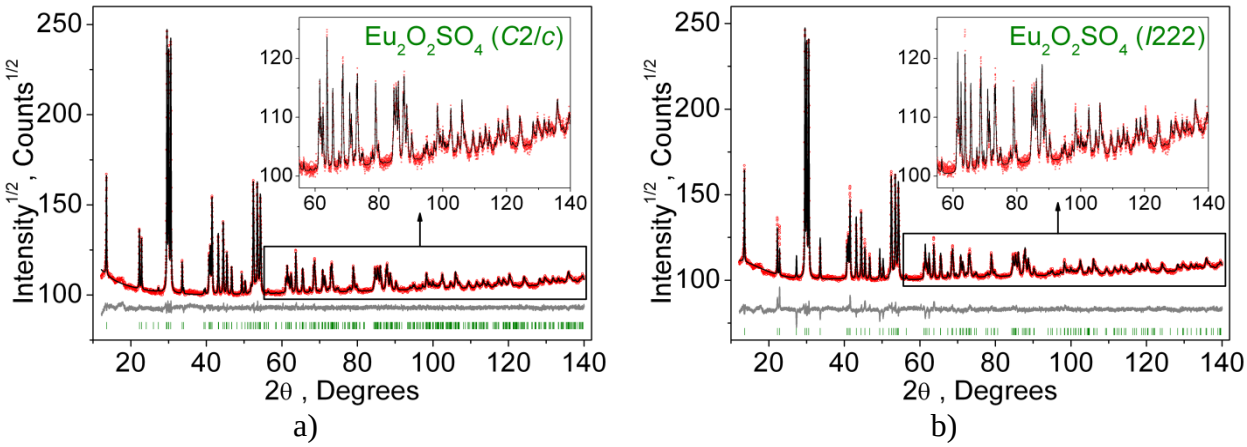
Eu2O2SO4 (C2/c)
Intensity1/2, Counts1/2
2θ , Degrees
a)
Eu2O2SO4 (I222)
Intensity1/2, Counts1/2
2θ , Degrees
b)

Fig. 5

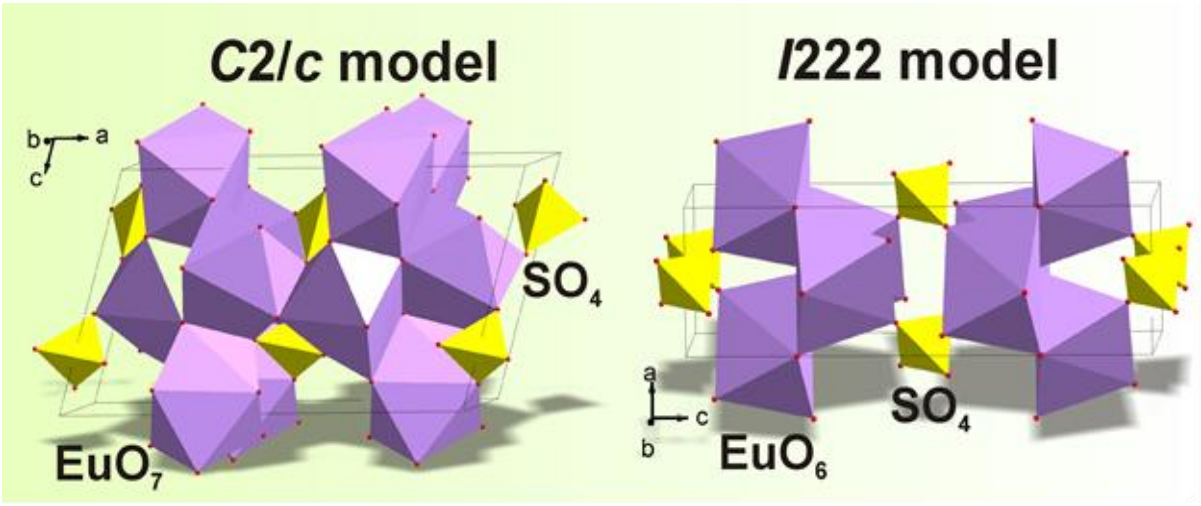

Fig. 6

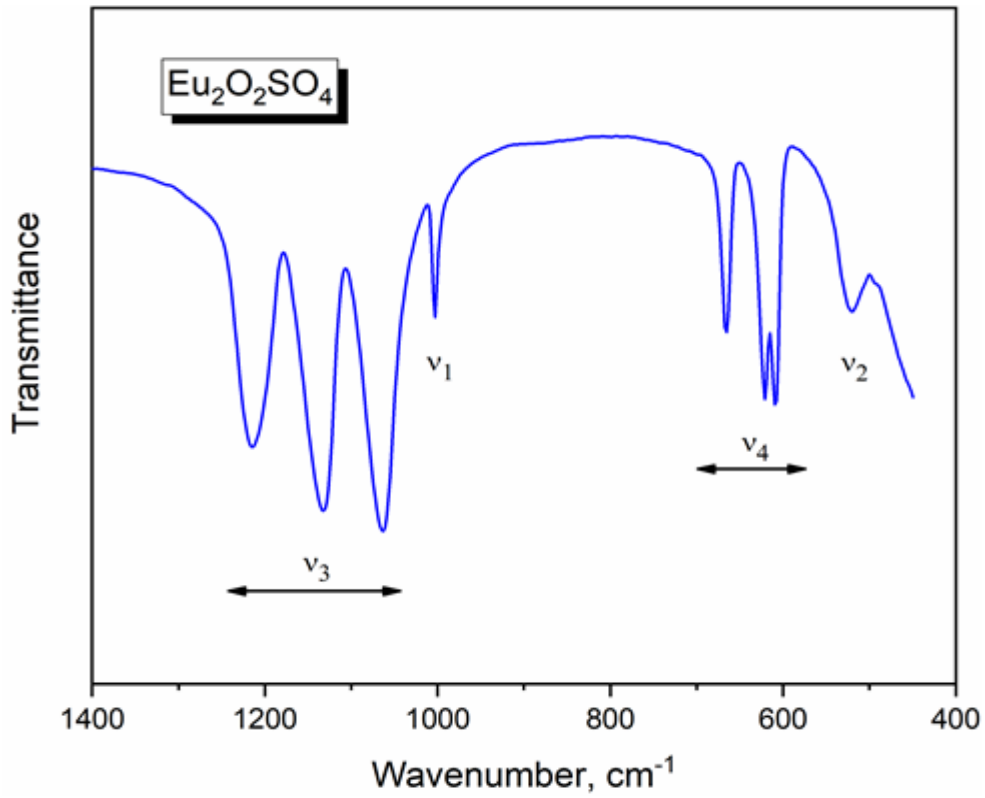
Eu2O2SO4
Transmittance
ν1
ν2
ν3
ν4
1400
1200
1000
800
600
400
Wavenumber, cm-1

Fig. 7

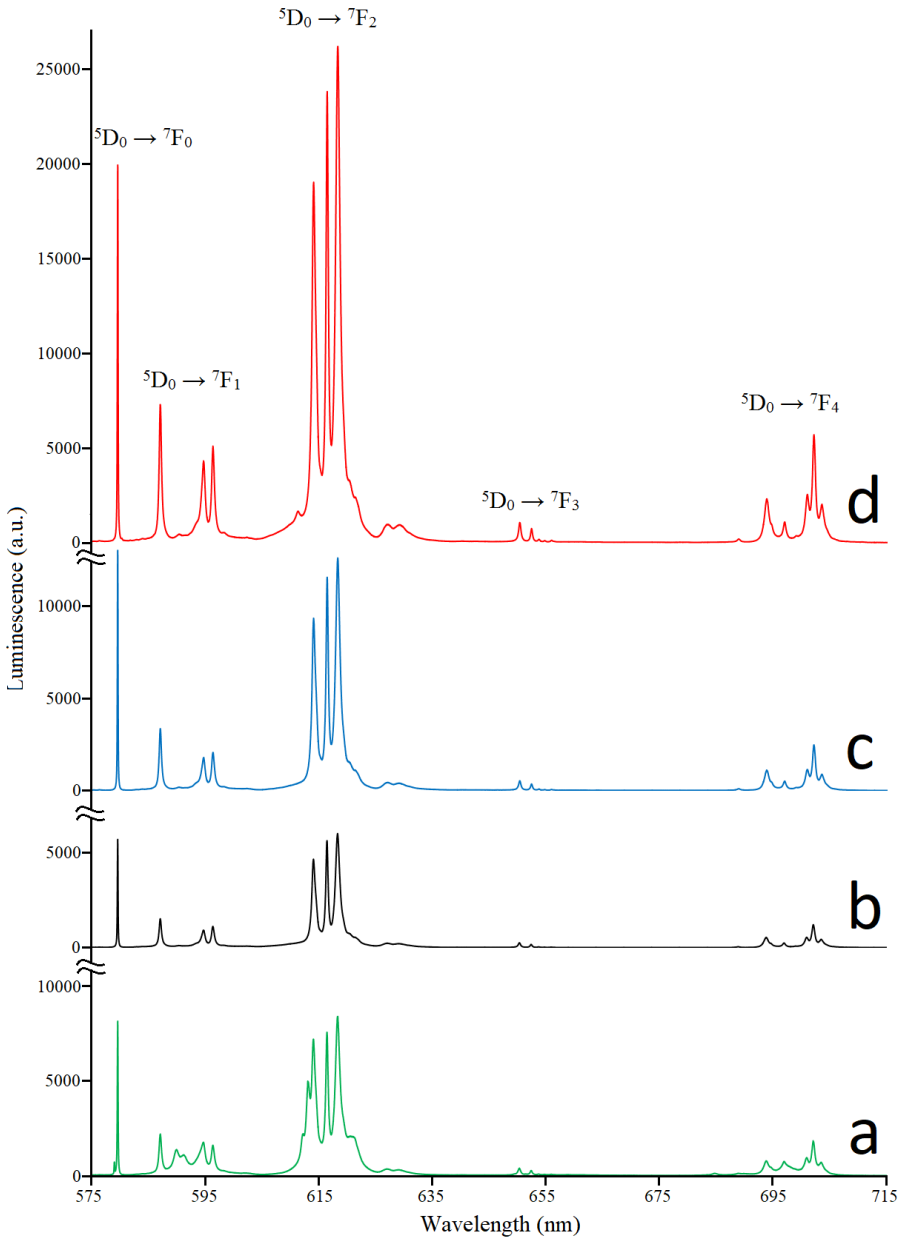
$^5D_0 \rightarrow {}^7F_2$
$^5D_0 \rightarrow {}^7F_0$
$^5D_0 \rightarrow {}^7F_1$
$^5D_0 \rightarrow {}^7F_3$
$^5D_0 \rightarrow {}^7F_4$
d
c
b
a
Luminescence (a.u.)
Wavelength (nm)
25000
20000
15000
10000
5000
0
575
595
615
635
655
675
695
715

Fig. 8

Tables

Table 1. Main parameters of processing and refinement of the $Eu_2O_2SO_4$ sample

Compound	$Eu_2O_2SO_4$	
Sp.Gr.	*C*2/*c*	*I*222
a, Å	13.6583 (3)	4.0716 (1)
b, Å	4.18874 (7)	4.1883 (1)
c, Å	8.1440 (1)	13.0412 (3)
β, º	107.292 (2)	–
V, Å^3	444.89 (2)	222.393 (9)
Z	4	2
2θ-interval, º	12-140	12-140
No. of refined structural parameters	16	8
R_{wp}, %	1.37	1.77
R_p, %	1.04	1.25
R_{exp}, %	0.93	0.93
χ^2	1.47	1.90
R_B, %	0.26	1.21

Table 2. Correlation diagrams for internal vibrations of SO_4 tetrahedra in the *C*2/*c* and *I*222 structural models for $Eu_2O_2SO_4$

*C*2/*c* model			
Wavenumber, cm^{-1} [1]	T_d Point group	C_2 Site symmetry	C_{2h} Factor group symmetry
983	A_1 (ν_1)	A	$A_g + A_u$
450	E(ν_2)	$2A$	$2A_g + 2A_u$
1105	E(ν_3)	$A + 2B$	$A_g + A_u + 2B_g + 2B_u$
611	E(ν_4)	$A + 2B$	$A_g + A_u + 2B_g + 2B_u$
*I*222 model			
Wavenumber, cm^{-1} [1]	T_d Point group	D_2 Site symmetry	D_2 Factor group symmetry
983	A_1 (ν_1)	A	A
450	E(ν_2)	$2A$	$2A$
1105	E(ν_3)	$B_1+B_2+B_3$	$B_1+B_2+B_3$
611	E(ν_4)	$B_1+B_2+B_3$	$B_1+B_2+B_3$